Sahlgrenska Academy

Dosimetric impact of system specific geometric distortion on head and neck treatment plans in MRI only based radiation therapy

M. Sc. Thesis

Jesper Browall

Thesis:	30 hp
Program:	Medical physics program
Level:	Second Cycle
Semester/year:	Spring 2019
Supervisor:	Emilia Palmér, Maja Sohlin, Maria Ljungberg
Examiner:	Magnus Båth

Abstract

Thesis:	30 hp
Program:	Medical physics program
Level:	Second Cycle
Semester/year:	Spring 2019
Supervisor:	Emilia Palmér, Maja Sohlin, Maria Ljungberg
Examiner:	Magnus Båth

Background/ purpose: Because of the superior soft tissue contrast, in comparison with computed tomography (CT) data, magnetic resonance imaging (MRI) is of high interest to include in a larger extent in the radiation therapy (RT) process. In an MRI only workflow, the CT scan is excluded and a synthetic CT is used for treatment planning. This will spare the patient extra ionizing radiation alongside with the discomfort of two separate imaging scans. However, an awareness is that geometric distortions appear in the MRI data. If uncorrected, the distortions may translate into dosimetric errors. In this study, the MRI system specific distortions were quantified and investigated. Dosimetric effects caused by the geometric distortions on head and neck treatment plans were also evaluated.

Method: The MRI system specific distortion field was quantified by scanning a phantom using the clinically optimized pulse sequence in a 1.5 T MRI system. The inverted system specific distortion field was calculated and applied on the patient CT and RT structure data. Both the patient CT and RT structure data were transformed into the corresponding patient MRI frame of reference (FoR) before the inverted distortions were applied. The dosimetric effects of the system specific distortions were investigated by creating an optimized treatment plan on the distorted patient CT data. The optimized treatment plan was copied and recalculated on the undistorted patient CT data and the absorbed dose difference was analyzed in clinically relevant dose volume histogram (DVH) parameters.

Result: The mean geometric distortion for a radial distance of 200–250 mm from the MRI isocenter was 1.5 mm. The smallest and largest mean absorbed dose deviation was -0.19% and 1.1% for $D_{2\%}$ CTV_{68} and D_{mean} for right parotid gland, respectively.

Conclusion: In this study, the dosimetric impact of the MRI system specific distortions was found to have none, or only minor, clinical relevance for head and neck cancer treatment plans in an MRI only workflow.

Acknowledgments

I would like to offer my dearest thanks to my supervisors Emilia Palmér, Maja Sohlin and Maria Ljungberg for their patient guidance, enthusiastic encouragement and useful critiques of this research work. Thanks for passing your knowledge to me and for letting me know that taking a few steps back is a part of the progress and not to be seen as a failure. I would also like to thank Anna Karlsson for her great advice regarding writing this report. My grateful thanks are also extended to Fredrik Nordström for helping me with the calculation of the inverse of the distortion field.

Finally, I wish to thank my parents for their endless support during my studies.

Abbreviations

B_0	Static magnetic field
CT	Computed Tomography
CTV	Clinical Target Volume
DICOM	Digital Imaging and Communications in Medicine
DVH	Dose Volume Histogram
fMRI	Functional Magnetic Resonance Imaging
FoV	Field of View
FoR	Frame of Reference
GTV	Gross Tumor Volume
MRI	Magnetic Resonance Imaging
NRRD	Nearly Raw Raster Data
OAR	Organ(s) At Risk
PRV	Planning organ at risk volume
PTV	Planning Target Volume
RED	Relative Electron Density
RS	Radiotherapy Structure
RT	Radiotherapy
sCT	Synthetic CT
SNR	Signal to Noise Ratio
SD	Standard Deviation
VMAT	Volumetric Modulated Arc Therapy

Contents

1 Introduction

Every year, about 60 000 new cases of cancer are reported in Sweden and approximately 1 300 of them are head and neck cancer (Bergman et al., 2018). In order to cure or palliate the patient, external beam radiation therapy has been concluded to be beneficial for almost 80% of the cases (Delaney et al., 2005).

Because of the superior soft tissue contrast, in comparison with computed tomography (CT) data, magnetic resonance imaging (MRI) is being used to a greater extent in the radiotherapy (RT) departments than before. The excellent contrast is favorable for delineation of tumor(s) and organ(s) at risk (OAR). Because of this advantage compared to CT data, together with the possibilities of additional applications such as functional MRI (fMRI), MRI data will most likely have an even bigger role in the RT process in the future (Blomqvist et al., 2013). For treatment planning, CT data are being used because of the high spatial accuracy and the relative electron density (RED) information. Both of these properties are crucial in the RT treatment planning process in the RT workflow. However, MRI data for tumor delineation have advantages. The gross tumor volume (GTV) for nasopharyngeal carcinoma was on average significantly larger compared to GTVs outlined on patient CT data (Emami et al., 2003). This means that the GTV delineated on patient CT data were consistently outlined smaller than they should be, according to the MRI data.

The problem with inaccurate tumor and OAR delineation that arises from using the CT data is solved by a combined workflow with both CT and MRI data. The CT data provide the RED information for absorbed dose calculation and the MRI data grant the soft tissue contrast and are utilized for the delineation of tumor volumes and OARs. This kind of workflow requires a registration between the MRI and CT data in order to get a common frame of reference (FoR). The registration can give rise to increased spatial uncertainty and therefore a different absorbed dose distribution than intended to the patient (Nyholm et al., 2009). By excluding the CT data from the RT process it would create a so-called "MRI only" workflow. The exclusion of CT data would also eliminate the registration between the two modalities and thereby the spatial uncertainties it entails. There are more reasons why an MRI only workflow is beneficial as well. Not only does it spare the patient the absorbed dose from a CT scan, but it would also ease the patient discomfort using only one imaging modality. It may also save the treatment facility time, effort and resources spent per patient. An MRI only workflow is also favorable in adaptive radiation therapy, where the daily treatment plan is based on the tumor location in real-time while the patient is on the treatment couch (Lamb et al., 2017). In order to achieve an MRI only workflow, different methods have been suggested for extraction of the RED directly from the MRI data and creating so-called "synthetic CT" (sCT) data (Kazemifar et al., 2019; Farjam et al., 2017; Siversson et al., 2015; Paulus et al., 2015; Andreasen et al.,

2015; Hsu et al., 2013).

Geometric distortion appears in all MRI data to a certain extent and has to be considered when used for treatment planning and delineation of tumors and OARs. If uncorrected, the distortions may translate into dosimetric errors (Weygand et al., 2016). The geometric distortions in MRI data can be divided into two separate types; system specific and patient/object specific. The system specific distortions originate from inhomogeneous static magnetic field (B_0) and/or non-linear gradients. The patient/object distortions originate from differences in susceptibility and/or chemical shifts (Bakker et al., 1992). There are several techniques to compensate for the patient/object induced distortions, such as field inhomogeneity mapping, (Wang et al., 2013; Jezzard and Balaban, 1995; Robson et al., 1997), usage of shimming coils (Weygand et al., 2016) and an increased bandwidth (Bakker et al., 1992).

The magnitude of the system specific distortions increases with the distance from the MRI isocenter (Gustafsson et al., 2017; Walker et al., 2014; Wang et al., 2004) and is therefore strongly dependent on the size of the Field of View (FoV). The gradient non-linearity is the main source for the geomtric distortions (Jafar et al., 2017; Baldwin et al., 2007). The different MRI system manufactures have different algorithms available which, to some extent, corrects the system related distortions (Walker et al., 2014). But geometric distortion is never completely removed.

When measuring the geometric distortions generated from the MRI system, it is common to use a phantom with some sort of signal producing objects placed in a grid or another pattern (Adjeiwaah et al., 2018; Baldwin et al., 2007; Jafar et al., 2017). The magnitude of the distortions is stated as the difference between where the grid/markers should be and where they appear in the MRI data. There are other phantoms measuring the geometric distortion as well, such as cylindrical rods and capillary tubes. If an MRI only workflow is to be used, the maximum geometric distortions should not exceed 2 mm (Weygand et al., 2016).

The effects of geometric distortions in an MRI only workflow with respect to absorbed dose distributions have been investigated for different anatomical sites, e.g. the brain (Dinkla et al., 2018; Wiesinger et al., 2018; Stanescu et al., 2008), breasts (Walker et al., 2016), prostate (Gustafsson et al., 2017; Adjeiwaah et al., 2018) and lungs (Wang et al., 2017). Promising results have been reported for head and neck cancer (Adjeiwaah et al., 2019). However, further investigations are needed for different MRI systems.

The aim of this study was to quantify and investigate the geometric distortions originating from the MRI system dedicated for RT and to evaluate the dosimetric effects that the geometric distortions may have on the absorbed dose distributions for head and neck cancer treatment plans.

2 Materials and methods

This study was divided into five different parts where the first part was characterization of the MRI system specific distortion field. The second part was to transform patient CT data (from now on referred to as "CT data") to the corresponding MRI data FoR. The third part was to apply the MRI system specific distortion field on the CT data and the fourth part to transform and distort the delineated RT structures, i.e. the volumes of interest. The last part was to simulate an MRI only workflow and investigate the dosimetric effects of the system specific geometric distortions using data from 10 head and neck cancer patients previously treated at the department. An illustration of the workflow can be found in figure 1.

2.1 Data acquisition and characterization of the distortion field

The study was approved by the regional ethical review board in Gothenburg, Sweden (645-17). Data from 10 head and neck cancer patients were included in this study. The data consisted of six men and four women with an age span of 50-77 years (average 64 years) and weighing 61-102 kg (average 75 kg). The inclusion criterion was a good correspondence between the new locations of the RT structures relative to the CT data after performing a rigid registration between the CT and MRI data. The correspondence was better when the deviations of the locations of large bone structures, such as the spine and skull, were small.

The 3D phantom (GRADE, Phantom number TS1006) used in this study is designed to estimate the geometric distortions in large FoV MRI data and is commercially available (Spectronic Medical AB, Helsingborg, Sweden). The phantom contained 1056 spherical markers with a diameter of 17 mm which were filled with polyethylene glycol (figure 2). The grid of the markers covered a volume of $429 \times 334 \times 470$ mm^3. The MRI system (Siemens 1.5 T, Erlangen, Germany) is dedicated for RT at Sahlgrenska University Hospital. The system has a bore width of 70 cm. The CT data included in this study were acquired using a Toshiba Aquilion LB CT scanner (Toshiba Medical Systems, Ōtawara, Japan). The slice thickness was 2 mm, the reconstruction diameter was 498-550 mm, the peak kilo voltage output was 120 kV and the exposure was 225 mAs.

The MRI pulse sequence utilized for the patient data was also used when scanning the phantom in order to accurately establish the geometric distortions and their effect in an MRI only workflow for head and neck cancer patients.

The phantom was placed on the patient couch without using the flat table top (figure 3). The Dixon pulse sequence clinically optimized for head and neck cancer was used along with the built in body coil. The data was assigned using a scan

matrix (frequency×phase) 448×381, reconstruction matrix (frequency×phase) 448×448, reconstruction FoV 500×500 mm, repetition time: 8 ms, echo time: 4.8 ms and 2.4 ms, slice thickness 2 mm, slice spacing 0 mm, number of slices 192, number of averages 32, total scan time 4 h 42 min 34 s and bandwidth 795 Hz/pixel. Clinically for patient data the number of averages was 3 and total scan time was 9 min 59 s. The longer scan time and greater number of averages for the phantom was used due to increase the signal to noise ratio (SNR).

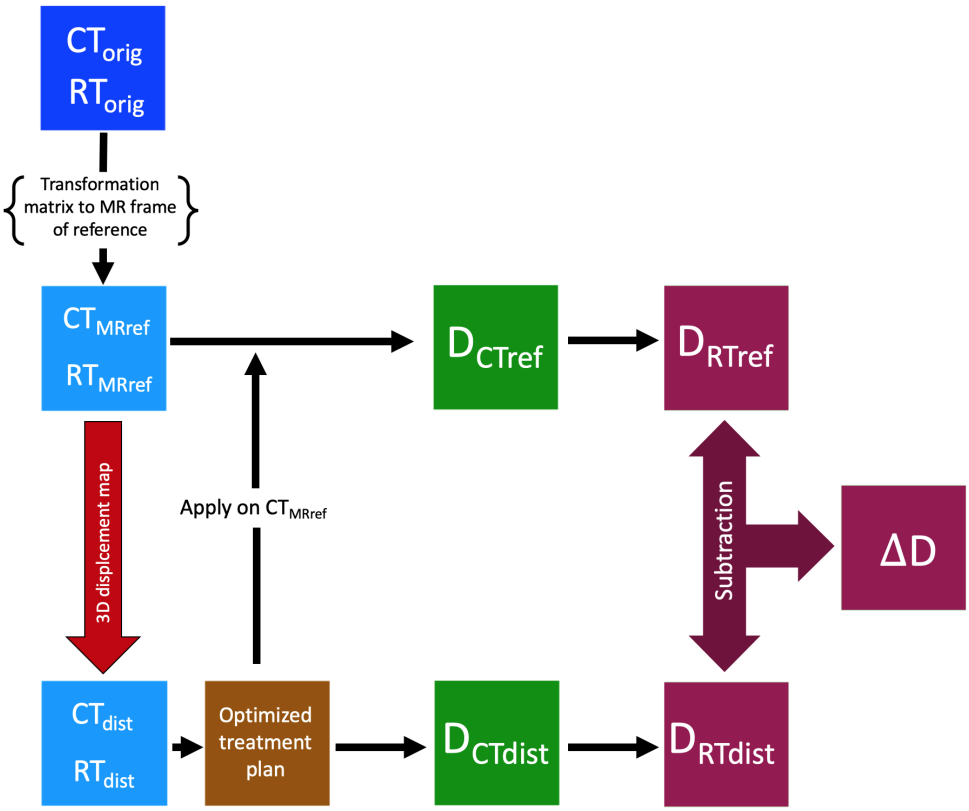

Figure 1: Illustration of the study workflow. CT_{orig}=original CT data, RT_{orig}=original RT structure data, CT_{MRref}=CT data in the corresponding MRI data FoR, RT_{MRref}=RT structures in their corresponding MRI data FoR, CT_{dist}=distorted CT data, RT_{dist}=distorted RT structures, D_{CTdist}=absorbed dose distribution calculated for CT_{dist}, D_{CTref}=absorbed dose distribution recalculated for CT_{MRref}, D_{RTdist}=absorbed dose for DVH parameters corresponding to the deformed RT structures, D_{RTref}=absorbed dose for DVH parameters corresponding to the none-deformed RT structures, ΔD=relative absorbed dose difference between DVH_{RTdist} and DVH_{RTref}. Note that the 3D displacement map is the iteratively calculated inverse of the distortion field received from the GRADE software.

The system specific distortion field was calculated using a cloud-based analysis

software. (GRADE version 1.0.46, Spectronic Medical AB, Helsingborg, Sweden). This software calculates the position of the sphere markers in the phantom MRI data via a non-rigid registration between the phantom MRI data and a digital reference model of the phantom. Reference markers with the "true" positions where generated from the digital reference phantom via a rigid registration between the model and the phantom MRI data using only slices close to isocenter, where the distortions are assumed to be negligible. For each of the markers, the difference in position between the reference markers and the markers generated from the non-rigid registration was calculated. The system specific distortion field was calculated with inverse mapping (Beier and Neely, 1992) and returned as a 4D matrix, i.e. data with displacement in the x-, y- and z-direction for the entire data volume scanned. The voxel dimensions for the matrix was 1.00 mm $\times$ 1.00 mm $\times$ 1.00 mm. Aside from the system specific distortion field, a binary mask containing ones where markers were detected were also received from the GRADE software alongside with text files containing data from where the mass centers of the markers where detected and where their "true" positions were. In order to exclude non-reliable data, the binary mask was applied to the system specific distortion field.

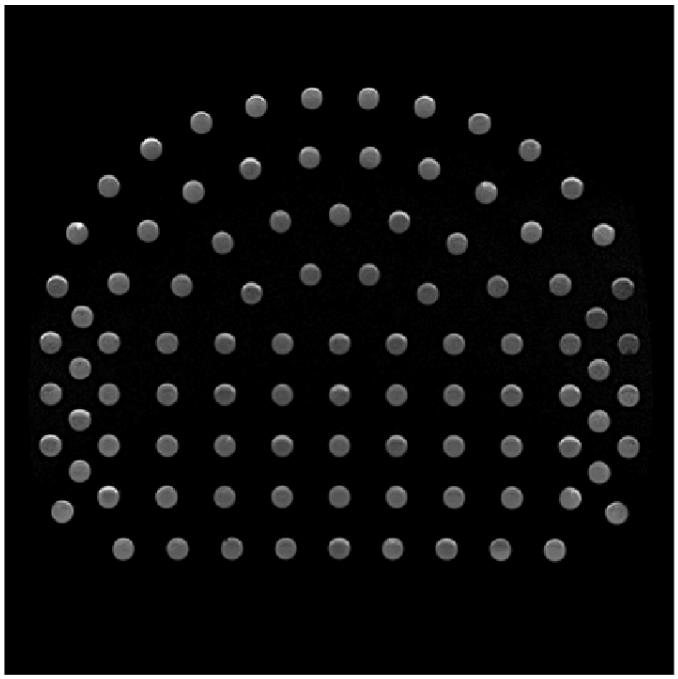

Figure 2: MRI data representing a transversal slice of the GRADE phantom where the spherical markers are shown in gray.

The system specific distortion field received from the GRADE software can be used as a correction for distortions in the MRI data. Hence, the inverse of the received distortion was generated to correctly distort the included CT data sets in order to simulate an MRI only workflow with the system specific distortion in consideration. The inverse was calculated iteratively by using InvertDisplacementFieldImageFilter in Simple ITK[1] 0.9.0 (open-source) together with ITK 4.7.2. To verify the existence of an inverse matrix, the determinant of the Jacobian of the system specific distortion field was investigated. The value of zero correlates to non-invertable data and negative values indicates non-invertable and unrealistic distortions (Chen et al., 2008; Veiga et al., 2015). The determinant was calculated after applying the binary mask to the deformation field. From now on, the inverse of the distortion field is denoted the 3D displacement map (figure 1).

Figure 3: The 3D GRADE phantom (Spectronic Medical AB)placed on the couch without the flat table top.

2.2 Transforming CT data to the MRI data FoR

In order to correctly apply the 3D displacement map on the CT data, the CT data must be in the same FoR as the corresponding MRI data. This was achieved with an in-house developed MATLAB-script (Version R2018a 9.4.0, The MathWorks Inc., Natick, Massachusetts, USA) in combination with an open access software (Convert3D, Version 1.0, ITK-SNAP). The MATLAB-script extracted the transformation matrix from the clinical rigid registration between the CT

[1]http://www.simpleitk.org, 2019-05-25

data and the corresponding MRI data. The registration was done in Eclipse treatment planning system (Varian Medical Systems, Version 15.6, Palo Alto, CA, USA). The transformation matrix was then exported as a text file and used in Convert3D alongside with the CT and MRI data. In order to use the CT and MRI data in Convert 3D, the data needed to be converted from Digital Imaging and Communications in Medicine (DICOM) to Nearly Raw Raster Data (NRRD) format. This was accomplished using Slicer[2] (Version 4.10.1). After the data was processed in the Convert3D software, the CT data had the same voxel size, FoV and FoR as the corresponding MRI data and are from now on referred to as the CT_{MRref} (figure 1). The CT_{MRref} data was then converted back to DICOM format using Slicer.

2.3 Applying the 3D displacement map on CT data

By using an in-house developed MATLAB-script, the 3D displacement map was linearly downsampled to match the pixel dimensions of the CT_{MRref} data. The magnitude of the system specific geometric distortion for each separate spatial direction was extracted from the 3D displacement map. The information regarding the CT_{MRref} data positions with respect to the MRI isocenter was extracted using the DICOM data from the corresponding MRI data. The positions of the 3D displacement map slices were extracted from their metadata. To ensure that the 3D displacement map was applied correctly in the superior-inferior direction, the CT_{MRref} and the 3D displacement map slice locations were compared and the 3D displacement map was then linearly interpolated to match the nearest CT_{MRref} slice. In the anterior-posterior and left-right direction the 3D displacement map was applied by knowing the difference in the isocenter position in the x- and y-direction for both the MRI data and the 3D displacement map. A translation of the 3D displacement map was applied corresponding to this difference and was then linearly interpolated. CT data outside the binary mask of the distortion field were left undistorted. The 3D displacement map was applied as a geometric transformation using linear interpolation and the resulting distorted CT data is from now on referred to as CT_{dist} (figure 1).

2.4 Distortion of RT structures

The RT structures that were transformed/distorted were clinically relevant dose volume histogram (DVH) parameters (table 1). Some specific structures that were based on the tumor localisation needed for treatment planning were also transformed/distorted. The body structure was re-delineated using the auto segmentation tool in the treatment planning system. The distortion of the RT

[2]https://www.slicer.org, 2019-05-25

structures was accomplished using an in-house developed MATLAB-script by utilizing the RS (Radiotherapy Structure) DICOM file exported from Eclipse treatment planning system. The relative orientation of the displacement data and the RT structure data, that was defined in x-, y- and z-coordinates with respect to their corresponding CT data, was taken into account by applying the transformation matrix. This is the same as used in section 2.2. The RT structure data created is referred to as RT_{MRref} (figure 1). After being transformed to the corresponding MRI FoR, all structure coordinates were translated into a position in the 3D displacement map. Since the coordinate often did not match an exact voxel in the 3D displacement map, the distortion was extracted using linear interpolation. The distortion was applied on the RT structure coordinates, creating RT_{dist} (figure 1), and new structure sets was written and saved as a new RS DICOM file. The new RS DICOM file was then imported to the treatment planning system.

2.5 Treatment planning and dosimetric analysis

In this study, all treatment planning was done by a medical physics student with instructions from an experienced clinical medical physicist using volumetric modulated arc therapy (VMAT) with 6 MV beams. The anisotropic analytical algorithm (AAA) (Version 13.6.23) and a 2.5 mm $\times$ 2.5 mm grid was used for dose calculation. The prescribed dose to the patients included was 68 Gy. In order to properly simulate an MRI only workflow with the system specific distortions in consideration, all treatment planning was achieved using RT_{dist} and the CT_{dist} data. This resulted in D_{CTdist} and D_{RTdist} (figure 1). The created treatment plans were aimed to be clinically relevant and fulfilling the same treatment planning criteria as the original clinical treatment plan. However, some exceptions were made due to imperfect registrations between the CT an MRI data. For these imperfect registrations the RT structures ended up in locations that were not anatomical correct. All treatment planning was accomplished in the Eclipse treatment planning system and the optimization parameters from the original clinical treatment plan was used as a template with only minor modifications. The created treatment plan was copied and recalculated in the CT_{MRref} geometry, creating a reference absorbed dose distribution D_{CTref} and a reference absorbed dose to RT structures D_{RTref}.

The RT structures evaluated was; clinical target volume (CTV) for 68 Gy and 52.7 Gy (CTV_{68} and $CTV_{52.7}$), planning organ at risk volume (PRV) spinal cord, parotid glands (left and right), larynx, esophagus upper, submandibularis (left and right) and body. The DVH parameters for the different structures that were evaluated were chosen from a randomized multicenter phase III study (ARTSCAN III) (available in the appendix) aside from the ones associated to CTV_{68} and $CTV_{52.7}$ (Gebre-Medhin, 2013). $D_{98\%}$ and $D_{2\%}$ for CTV_{68} were copied

from the PTV (Planning Target Volume) criteria due to that the PTV for the data sets included in the study was delineated outside the body contour and thus making it impossible to fulfill. D_{mean} for CTV_{68} was added because it was of interest to examine the the difference in absorbed dose delivered to the tumor. $D_{98\%}$ for $CTV_{52.7}$ was added since some patients were prescribed 52.7 Gy and was copied with the same corresponding absorbed dose as the PTV 54.4 from the ARTSCAN III protocol (Gebre-Medhin, 2013). All DVH parameters investigated can be seen in table 1.

Table 1: DVH parameters investigated for the different RT structures of interest and number of data sets included in the study. D_{mean}=mean absorbed dose, $D_{98\%}$=near minimum absorbed dose that 98% of the volume receives, $D_{2\%}$=near maximum absorbed dose that 2% of the volume receives, D_{max}=maximum absorbed dose.

RT structure	**Parameter**	**Patients included**
PRV Spinal cord	$D_{2\%}$	10
CTV_{68}	D_{mean}	10
	$D_{98\%}$	10
	$D_{2\%}$	10
$CTV_{52.7}$	$D_{98\%}$	8[1]
Parotid left	D_{mean}	9[2]
Parotid right	D_{mean}	10
Larynx	D_{mean}	10
Upper esophageal sphincter	D_{mean}	10
Submandibularis left	D_{mean}	8[2]
Submandibularis right	D_{mean}	10
Body	D_{max}	10

[1]Not prescribed
[2]Surgically removed

The relative absorbed dose difference for DVH parameters of interest was calculated for the chosen RT structures for each of the data sets according to

$$\Delta D(\%) = \frac{D_{RTdist} - D_{RTref}}{D_{RTdist}} \cdot 100, \tag{1}$$

where ΔD is 3D absorbed dose differences except for the parameter D_{max}, which is a point (table 1).

3 Results

MRI system specific geometric distortions were successfully investigated and the dosimetric effect for head and neck treatment plans were evaluated.

3.1 Evaluation of the 3D displacement map

The proportion of voxels in the distortion field with a corresponding Jacobian determinant being less than 0 was 0.05%. These voxels were generally located in the most peripheral part of the phantom. No voxels had a corresponding Jacobian determinant being equal to zero.

3.2 Geometric distortion measurements

The absolute value of mean, minimum and maximum geometric distortion of the phantom in three different spatial directions (left-right, anterior-posterior and inferior-superior) was calculated (table 2). The distortion was largest in the left-right direction. The mean and maximum of the geometric distortion as a function of the radial distance from the MRI isocenter were evaluated (table 3). The magnitude of the distortion was found to increase with increased distance from the MRI isocenter, with large spread of the data (figure 4). One slice of the 3D displacement map close to the MRI isocenter is displayed (figure 5) It can be seen that the largest distortions are in the upper peripheral part of the phantom.

Table 2: The absolute value of mean, minimum and maximum geometric distortion of the phantom in the three different spatial directions. Distance covered by the spherical markers was 429, 334 and 385 mm in the left-right, anterior-posterior, inferior-superior direction, respectively. The mean value is presented with 1 standard deviation (SD).

Left-Right [mm]			Anterior-Posterior [mm]			Inferior-Superior [mm]		
Mean	Min	Max	Mean	Min	Max	Mean	Min	Max
0.52 ± 0.72	0.00	4.1	0.50 ± 0.68	0.00	4.0	0.42 ± 0.39	0.00	2.1

Table 3: Magnitude of mean and maximum geometric distortion [mm] for different distances from the MRI isocenter [mm].

<100		100–150		150–200		200–250	
Mean	Max	Mean	Max	Mean	Max	Mean	Max
0.37	1.3	0.51	1.7	0.78	3.2	1.5	4.2

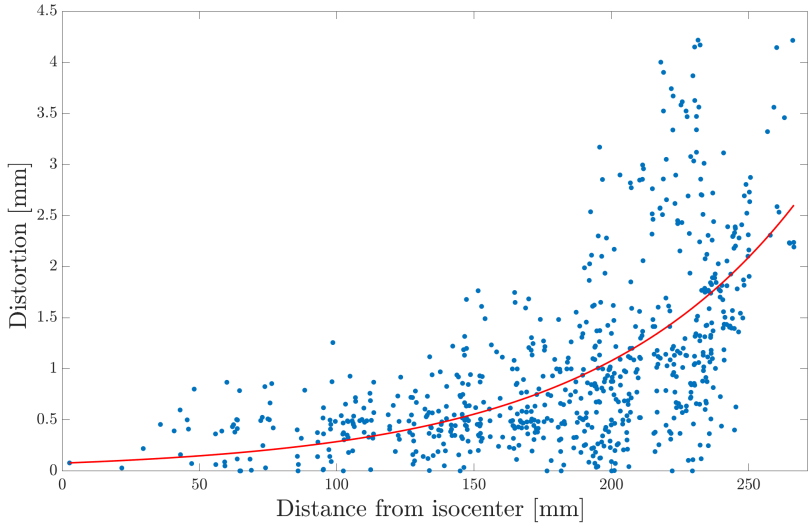

Figure 4: Magnitude of the geometric distortion as a function of distance from the MRI isocenter. The red line is a fitted exponential curve using all data.

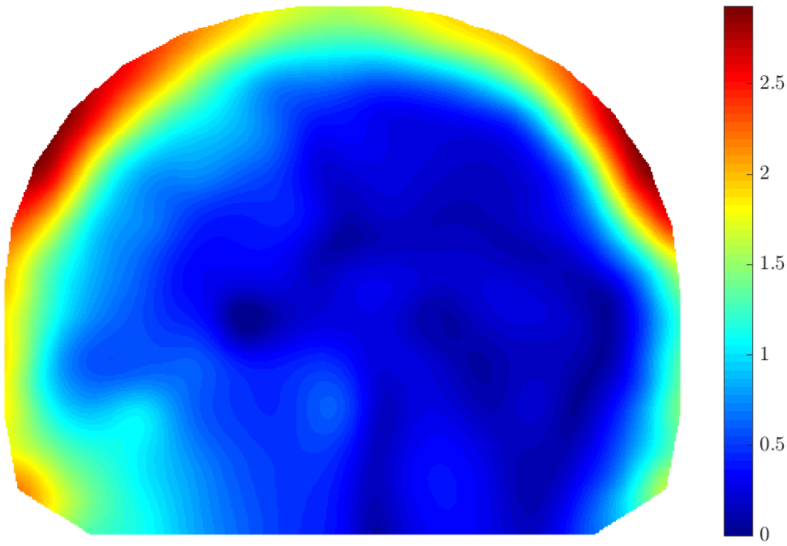

Figure 5: The magnitude of the distortions [mm] in one slice of the 3D displacement map close to the MRI isocenter.

3.3 Dosimetric impact on RT structures

The mean deviation between the distorted and undistorted RT structures was calculated in percent and absorbed dose for all volumes of interest and corre-

sponding specific DVH parameters (table 4). $D_{2\%}$ for CTV_{68} had the smallest mean deviation in both percent and absorbed dose with values of 0.019 % and 0.013 Gy, respectively. Right parotid gland had the largest deviation in mean percentage absorbed dose (1.1%) and upper esophageal sphincter had the largest deviation in absorbed dose (-0.39 Gy).

Table 4: Mean deviation between D_{RTdist} and D_{RTref} with one SD presented in percent and absorbed dose for all RT structures of interest and corresponding DVH parameters. The mean volume for the distorted RT structures with one SD is also presented.

RT structure	Param.	Mean deviation [%] (1 SD)	Mean deviation [Gy] (1 SD)	Volume [cm^3] (1 SD)
PRV Spinal cord	$D_{2\%}$	-0.083 (0.56)	-0.018 (0.21)	40 (9.3)
CTV_{68}	D_{mean}	0.039 (0.064)	0.026 (0.044)	160 (71)
	$D_{98\%}$	-0.042 (0.60)	-0.029 (0.39)	
	$D_{2\%}$	0.019 (0.068)	0.013 (0.048)	
$CTV_{52.7}$	$D_{98\%}$	-0.31 (0.43)	-0.15 (0.21)	87 (51)
Parotid left	D_{mean}	-0.16 (0.73)	-0.021 (0.15)	23 (7.7)
Parotid right	D_{mean}	1.1 (2.1)	0.35 (0.65)	24 (9.0)
Larynx	D_{mean}	-0.34 (0.72)	-0.12 (0.27)	26 (10)
Up. esophag. sph.	D_{mean}	-1.0 (3.3)	-0.39 (1.2)	3.7 (1.9)
Submandib. L	D_{mean}	0.24 (0.35)	0.11 (0.16)	8.4 (2.0)
Submandib. R	D_{mean}	-0.17 (0.39)	-0.033 (0.071)	8.1 (2.2)
Body	D_{max}	-0.078 (0.34)	-0.059 (0.26)	12 000 (2200)

The relative absorbed dose difference was calculated using equation 1. The data received from applying equation 1 on all RT structures of interest for all data sets was evaluated (figure 6). The largest local percentage difference, 11.8%, was observed for the mean absorbed dose to the upper esophageal sphincter. The corresponding smallest difference was found for the CTV_{68} with an absorbed dose difference of 0.21%. The majority of the minimum and maximum values in the box evaluations are within the ±1% margin. However, there are some major so-called "outliers" for the upper esophageal sphincter and right parotid gland (upper figure 6). All absorbed dose data can be found in the appendix.

The difference in absorbed dose distribution for CT_{dist} and CT_{MRref} was evaluated (figure 7). It was observed that the largest difference in absorbed dose is located in the lower anterior part of the shoulders with differences up to 26 Gy.

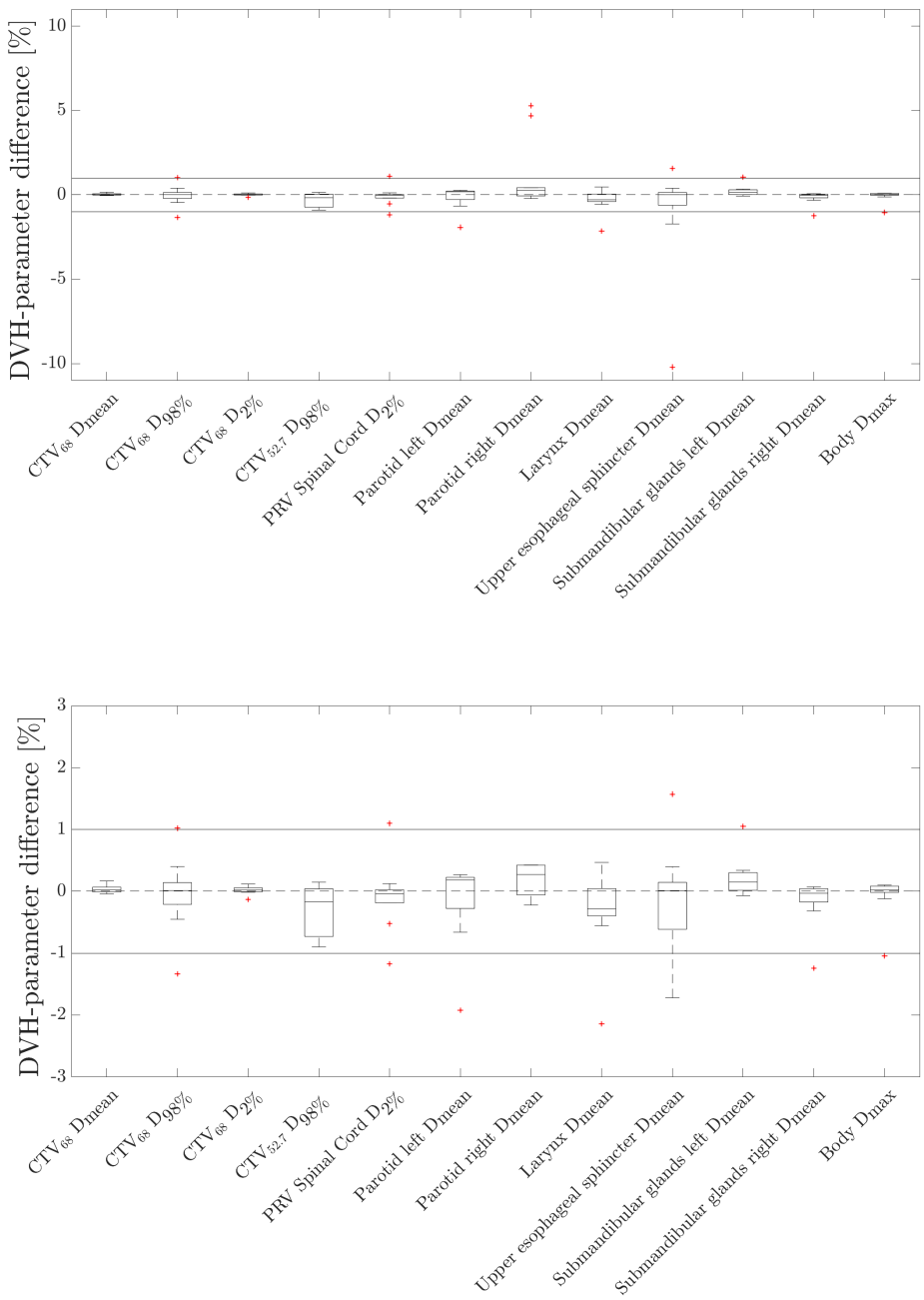

Figure 6: Upper: Boxplot of all the data received from the calculation of the relative absorbed dose difference between D_{RTdist} and D_{RTref}. Lower: cropped in order to properly illustrate the results. The horizontal line in the box is the median, the lower and upper part (q_1 and q_3) of the box represents the first and third quartile, respectively. The vertical dotted lines (whiskers) represents the highest/lowest value which are greater than $q_3 + 1.5 \cdot (q_3 - q_1)$ or less than q_1–$1.5 \cdot (q_3 - q_1)$. All data outside the whiskers are so-called "outliers". Two horizontal lines represents $\pm 1\%$.

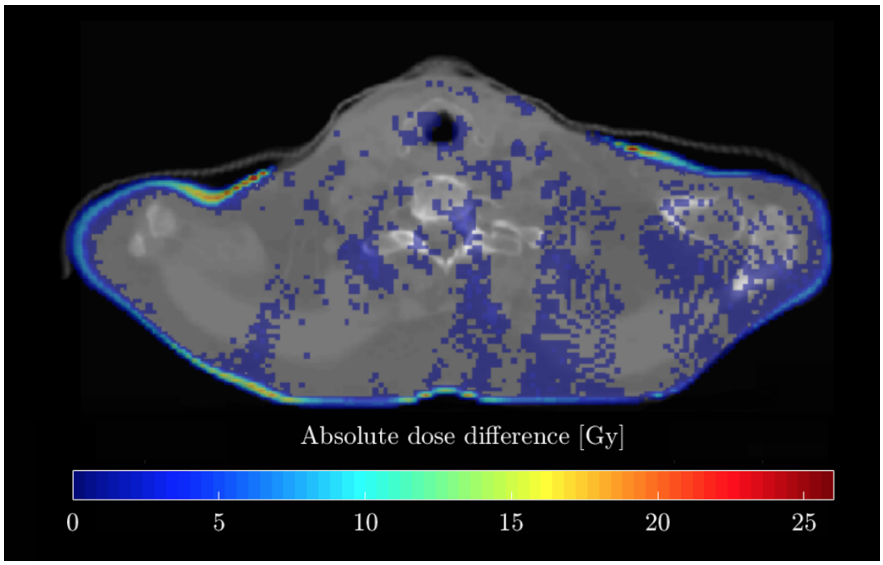

Figure 7: The absolute absorbed dose difference after subtracting the absorbed dose distribution D_{CTref} from D_{CTdist} in one slice of data set 2 and is thresholded to integers. The large dark blue area corresponds to circa 1 Gy absolute absorbed dose difference.

4 Discussion

The MRI system specific distortions in this study were characterized by using a geometrical phantom and a Dixon pulse sequence. As expected the distortions were larger with increased distance from the MRI isocenter (Gustafsson et al., 2017; Walker et al., 2014; Wang et al., 2004). Both the mean and maximum distortion was largest in the left-right direction for the volume scanned. Probably since that is the spatial direction with most coverage with respect to detected spherical markers.

The result is somewhat different compared to the result presented by Gustafsson et al., (2017). However, they did not use the same MRI system (3 T Discovery 750W, Software DV25R02-1549b, General Electric Healthcare, Milwaukee, WI) as we did and the bandwidth of the pulse sequence were different as well. There is though a considerable difference between the maximum distortion in all spatial directions investigated as well as the mean distortion in the left-right and anterior-posterior direction where the result in this study indicates generally larger distortions. The result shows the importance that each MRI system and MRI only pulse sequence is investigated since the character of the distortions may vary. The magnitude of the distortions with respect to the radial distance from the MRI isocenter is similar between the studies.

The dosimetric effect of the system specific distortions was assessed by cre-

ating an optimized treatment plan on distorted CT data with the corresponding distorted RT structures in the MRI FoR. The treatment plan was then copied on to the original CT data in the corresponding MRI FoR and the absorbed dose distribution was recalculated and absorbed dose difference was evaluated. The local absorbed dose difference in the selected DVH parameters for the RT structures was generally very small with a few exceptions, i.e. the so-called outliers. A 2% dosimetric deviation for the DVH parameters is the usual criterion for clinically acceptable results when accounting for both MRI system specific and patient specific induced distortions (Edmund and Nyholm, 2017). Since this study only investigated the MRI system specific distortions the ±1% margin was chosen. Our results are in line with studies of lung and rectal cancer (Wang et al., 2017, 2018). Though, when comparing results it is important to compare RT structures with the same relative distance to the MRI isocenter since the distortions are highly dependent of this parameter. Therefore, the CTV in this study was compared with the result for the PTV in the studies by Wang et al.. CTV is always enclosed by the PTV and hence both volumes are located close to the isocenter of the MRI system. Wang et al. included both the MRI system and patient specific distortions on both studies. This could explain the mean relative difference in $D_{98\%}$ between D_{RTdist} and D_{RTref} in CTV being smaller than in the PTV for the lung cancer study (Wang et al., 2017). The same argument applies on the rectal cancer study (Wang et al., 2018), where the box plot clearly shows that D_{mean} and $D_{2\%}$ for PTV have larger spread and that $D_{2\%}$ has a larger median difference, compared to our CTV.

The major outliers associated with right parotid gland, larynx and upper esophageal sphincter were investigated further as well as the outliers just above/under the ± 1% margin for CTV, PRV spinal cord and upper esophageal sphincter. The rest of the outliers were left without further evaluation since they corresponded to structures that have a low priority in the ARTSCAN III protocol (Gebre-Medhin, 2013). The main cause for the outliers corresponding to $D_{98\%}$ for CTV_{68} was probably due to the distortion causing the CTV to end up either closer, or farther away, from the body contour. CTV was in both these cases located only a few millimeters inside the body contour and was therefore in the build-up region for the 6 MV beam. Hence, the absorbed dose distribution in the CTV was sensitive for displacements. The outliers associated with PRV spinal cord, the lower one of right parotid gland and larynx are probably a result of distortions causing the structure ending up closer/farther away from $CTV_{68}/CTV_{52.7}$. Where ending up closer to the CTV results in getting closer to higher absorbed dose levels and thereby a positive value when calculating the relative absorbed dose difference. Ending up farther away from the CTV gives a negative value with the corresponding argument. The outlier at -10.2 % for upper esophageal sphincter structure is most likely due to that the distortion caused almost a whole extra layer in a low absorbed dose area as well as half of the top

layer to be moved from a high absorbed dose area. Since it is a relatively small structure, and that the location is in a high absorbed dose gradient, the difference in absorbed dose between the distorted and undistorted structure is substantial. However, no such obvious arguments explaining the outlier associated with the larger of the two of right parotid gland and the left parotid gland was found.

In this study, the local absorbed dose difference has been evaluated. This was due to it was of interest to examine how the value of the DVH parameters chosen from the ARTSCAN III protocol changed when simulating the effects of system specific distortions in an MRI only workflow (Gebre-Medhin, 2013). When analyzing the relative difference in absorbed dose, it requires consideration of the clinical relevance. The absorbed dose difference was normalized locally to D_{RTdist} and neither the prescribed dose nor the dose objective for that particular structure was taken into account. This leads to that large relative absorbed dose differences not necessarily need to be clinically relevant for the particular case. As an example, the outliers associated to the right parotid gland correspond to relative absorbed dose differences of 5.3% and 4.7%. This corresponds to a prescribed dose (D_{mean}) of 31.0 Gy instead of 32.8 Gy and 28.6 Gy instead of 30.0 Gy, respectively. The reason why the absorbed dose is this high is because the right parotid glands in these cases are located close to the target and have little to none clinical relevance since both are much over the clinical objective of 20 Gy (Gebre-Medhin, 2013). The same argument applies when analyzing the mean deviation for all RT structures examined. Even though right parotid gland and upper esophageal sphincter have a relatively high mean absorbed dose deviation of 1.1% and -1.0%, respectively, it only correspond to a mean absolute absorbed dose deviation of 0.35 Gy and -0.39 Gy, i.e. these differences cannot be considered as clinically relevant.

When quantifying the distortion field, the object specific distortions of the phantom were not taken into account. The phantom is designed to cause very small or negligible effects on the measured system specific distortion field. A previous study concluded that the object specific distortions, with B_0 inhomogenety included, were less than 0.5 mm for all radial distances within 250 mm from the MRI isocenter (Gustafsson et al., 2017). This effect is therefore negligible since the scan volume for the head and neck cancer patients in this study is $500 \times 500 \times 384$ mm^3.

The 3D displacement map was iteratively calculated and is thereby a numerical approximation. By computing its Jacobian determinant, it is possible to evaluate the accuracy of this approach. The results in this study showed that the non-positive values of the Jacobian determinant are located in the peripheral part of the phantom. In most CT data sets the data volume is considerably smaller than the phantom volume. Hence, the unreliable distortion data are outside of the FoV for the study data.

When applying the 3D displacement map on the CT data, it is accomplished

as correctly as possible with an error that is maximum 0.5 pixels (0.56 mm) in the left-right or anterior-posterior direction. This should have a minimum effect on the result since the 3D displacement map does not change significantly at those small variations in space.

The rigid registration between the CT and MRI data is not perfect and gives rise to displacement errors in the delineated RT structures. This error has the magnitude of a few millimeters and resulted in CTV's ending up very close to the body contour and PRV spinal cords ending up inside the vertebrae. This error was smaller the better the registration between the modalities was. That is why the correspondence between the two modalities after the registration was the main inclusion criterion in the study. Even though the displacement error was relatively large, the effect of this should have an insignificant impact on the result. This is due to the difference between the D_{RTdist} and D_{RTref} is analyzed and both of them withstand the same error in displacement since both of them are transformed into the same MRI FoR system. However, the error occurring from the rigid registration had an impact on the dose planning in a matter of being clinically relevant. The CTV RT structure sometimes ended up very close to the body contour and thus making $D_{98\%}$ criterion impossible to satisfy. This was the case for two of the data sets.

The PTV in our data sets was delineated outside the body contour, making it impossible to satisfy the objectives according to the ARTSCAN III protocol (Gebre-Medhin, 2013). This is why the PTV criteria from the ARTSCAN III protocol were copied to our CTV. This resulted in difficulties regarding evaluation of the treatment plan being clinically relevant. Also, even though all the parameters (except for $D_{98\%}$ for two data sets) fulfilled the same criteria as the original treatment plan, no evaluation regarding high/low absorbed dose areas were made.

The selection of RT structures to transform/distort was based on the clinical relevance of the structure. Relevant structures were those that either were chosen for absorbed dose evaluation or needed for treatment planning. The structures of interest for treatment planning were selected based on the original clinical plan. All the treatment planning in this study was based on the same optimization parameters as the corresponding original treatment plan. The treatment plan was accepted as clinically relevant if it fulfilled the same absorbed dose objectives as the original treatment plan. PTV was not selected to be evaluated because the volume of this structure was often outside the body contour.

Unlike CT data, the RT structures are not pixel values but coordinates that create a volume. This means that for displacements in the inferior-superior direction that do not exactly match the position of a new slice in the CT data, the RT structure data is projected to the closest slice available. Therefore, when transforming/distorting the RT-structures, there were some errors that could not be avoided in the inferior-superior direction and the largest error in this direc-

tion could be 1 mm since the slice thickness is 2 mm. This effect is for most cases insignificant but gives sometimes rise to large errors, especially when it is a structure that is dispersed only in few slices and/or is placed close to sharp absorbed dose gradients. An example of this is the outlier associated with upper esophageal sphincter with a value of -10.2 % and described in more detail earlier. Also, when the RT structures are assigned to the closest CT slice, the coordinates are scrambled with the ones already in that plane which means they needed to be sorted. This was "semi-automatically" accomplished with an in-house developed MATLAB-script. The script arranges the coordinates by nearest neighbour but that alone is not a general solution to form a shape that resembles the corresponding original RT structure. Therefore, all RT structures that were transformed/distorted needed to be visually reviewed, slice by slice. If the structures did not have a satisfying appearance, i.e. if they did not look natural with the slice above/under as a reference, some minor modification was made such as changing the starting point from which the first nearest neighbour was calculated. This is one of the reasons to why the body structure was not transformed/distorted, since the modifications that was possible could not arrange the body structure coordinates to look anatomically correct. Also, transforming/distorting the body structure would result in the body contour being displaced inside/outside the visual appearance of the body in the CT data due to the registration error. This would make the treatment planning more unreliable since it solely calculates the absorbed dose inside the body structure. Instead of transforming/distorting the body structure, it was re-delineated by using the auto segmentation tool in the treatment planning system. This resulted in that the CTV sometimes ended up closer to the body structure compared to the original CT data as mentioned earlier.

A study weakness is the limited data included. In order to get more reliable results, more sample data would be desirable. Especially since all data sets do not include all the organs of interest to enable a full data set in the evaluation of the selected selected ARTSCAN III DVH parameters. This study only accounts for the system specific distortions. For complete evaluation of geometric distortion impact on head and neck treatment plans in an MRI only workflow, both patient and object specific distortions have to be taken into account.

5 Conclusion

In the given method it was possible to investigate the geometric distortions originating from the MRI system. The MRI system specific distortions increased for increased radial distance from the MRI system isocenter. The distortions were biggest in the left-right direction. All the data, except for a few outliers and D_{mean} for upper esophageal sphincter, were within the ± 1 % margin. It was

concluded that the dosimetric impact of the system specific geometric distortion on absorbed dose to the RT structures of interest has none or very limited clinical relevance. This means that the system specific distortions do not need to be accounted for in treatment planning in an MRI only workflow on head and neck cancer patients. Future studies will include evaluation of object specific distortions.

References

Adjeiwaah, M., Bylund, M., Lundman, J. A., Karlsson, C. T., Jonsson, J. H., and Nyholm, T. (2018). Quantifying the effect of 3T magnetic resonance imaging residual system sistortions and patient-induced susceptibility distortions on radiation therapy treatment planning for prostate cancer. *International Journal of Radiation Oncology, Biology, Physics*, 100(2):317–324.

Adjeiwaah, M., Bylund, M., Lundman, J. A., Soderstrom, K., Zackrisson, B., Jonsson, J. H., Garpebring, A., and Nyholm, T. (2019). Dosimetric impact of MRI distortions: A study on head and neck cancers. *International Journal of Radiation Oncology, Biology, Physics*, 103(4):994–1003.

Andreasen, D., Van Leemput, K., Hansen, R. H., Andersen, J. A., and Edmund, J. M. (2015). Patch-based generation of a pseudo CT from conventional MRI sequences for MRI-only radiotherapy of the brain. *Medical Physics*, 42(4):1596–1605.

Bakker, C. J., Moerland, M. A., Bhagwandien, R., and Beersma, R. (1992). Analysis of machine-dependent and object-induced geometric distortion in 2DFT MR imaging. *Magnetic Resonance Imaging*, 10(4):597–608.

Baldwin, L. N., Wachowicz, K., Thomas, S. D., Rivest, R., and Fallone, B. G. (2007). Characterization, prediction, and correction of geometric distortion in 3 T MR images. *Medical Physics*, 34(2):388–399.

Beier, T. and Neely, S. (1992). Feature-based image metamorphosis. *Computer Graphics*, 26(2):35–42.

Bergman, O., Fredholm, L., Hont, G., Johansson, E., Ljungman, P., Munck-Wikland, E., Nahi, H., and Zedenius, J. (2018). Cancer i siffror 2018. *Socialstyrelsen, Cancerfonden*, 2018-6-10.

Blomqvist, L., Bäck, A., Ceberg, C., Enblad, G., Frykholm, G., Johansson, M., Olsson, L. E., and Zackrisson, B. (2013). MR in radiotherapy - an important step towards personalised treatment? *Report from SSM's scientific council on ionizing radiation within oncology.*

Chen, M., Lu, W., Chen, Q., Ruchala, K. J., and Olivera, G. H. (2008). A simple fixed-point approach to invert a deformation field. *Medical Physics*, 35(1):81–88.

Delaney, G., Jacob, S., Featherstone, C., and Barton, M. (2005). The role of radiotherapy in cancer treatment: Estimating optimal utilization from a review of evidence-based clinical guidelines. *Cancer*, 104(6):1129–1137.

Dinkla, A. M., Wolterink, J. M., Maspero, M., Savenije, M. H. F., Verhoeff, J. J. C., Seravalli, E., Išgum, I., Seevinck, P. R., and van den Berg, C. A. T. (2018). MR-only brain radiation therapy: Dosimetric evaluation of synthetic CTs generated by a dilated convolutional neural Network. *International Journal of Radiation Oncology, Biology, Physics*, 102(4):801–812.

Edmund, J. M. and Nyholm, T. (2017). A review of substitute CT generation for MRI-only radiation therapy. *Radiation Oncology*, 12(1):28.

Emami, B., Sethi, A., and JPetruzzelli, G. (2003). Influence of mri on target volume delineation and imrt planning in nasopharyngeal carcinoma. *International Journal of Radiation Oncology, Biology, Physics*, 57:481–488.

Farjam, R., Tyagi, N., Veeraraghavan, H., Apte, A., Zakian, K., Hunt, M. A., and Deasy, J. O. (2017). Multiatlas approach with local registration goodness weighting for MRI-based electron density mapping of head and neck anatomy. *Medical Physics*, 44(7):3706–3717.

Gebre-Medhin, M. (2013). EU Clinical Trials Register. ARTSCAN III, A randomized multicenter phase III study of cisplatin plus radiotherapy compared to cetuximab plus radiotherapy in locally advanced head and neck cancer. Available from: https://www.clinicaltrialsregister.eu/ctr-search/trial/2012-001879-37/SEA [2019-06-26].

Gustafsson, C., Nordstrom, F., Persson, E., Brynolfsson, J., and Olsson, L. E. (2017). Assessment of dosimetric impact of system specific geometric distortion in an MRI only based radiotherapy workflow for prostate. *Physics in Medicine Biology*, 62(8):2976–2989.

Hsu, S. H., Cao, Y., Huang, K., Feng, M., and Balter, J. M. (2013). Investigation of a method for generating synthetic CT models from MRI scans of the head and neck for radiation therapy. *Physics in Medicine Biology*, 58(23):8419–8435.

Jafar, M., Jafar, Y. M., Dean, C., and Miquel, M. E. (2017). Assessment of geometric distortion in six clinical scanners using a 3D-printed grid phantom. *Journal of Imaging*, 3(3):28.

Jezzard, P. and Balaban, R. S. (1995). Correction for geometric distortion in echo planar images from B0 field variations. *Magnetic Resonance Imaging*, 34(1):65–73.

Kazemifar, S., McGuire, S., Timmerman, R., Wardak, Z., Nguyen, D., Park, Y., Jiang, S., and Owrangi, A. (2019). MRI-only brain radiotherapy: Assessing the dosimetric accuracy of synthetic CT images generated using a deep learning approach. *Radiotherapy and Oncology*, 136:56–63.

Lamb, J., Cao, M., Kishan, A., Agazaryan, N., Thomas, D. H., Shaverdian, N., Yang, Y., Ray, S., Low, D. A., Raldow, A., Steinberg, M. L., and Lee, P. (2017). Online adaptive radiation therapy: Implementation of a new process of care. *Cureus*, 9(8):1618.

Nyholm, T., Nyberg, M., Karlsson, M. G., and Karlsson, M. (2009). Systematisation of spatial uncertainties for comparison between a MR and a CT-based radiotherapy workflow for prostate treatments. *Radiation Oncology*, 4:54.

Paulus, D. H., Quick, H. H., Geppert, C., Fenchel, M., Zhan, Y., Hermosillo, G., Faul, D., Boada, F., Friedman, K. P., and Koesters, T. (2015). Whole-body PET/MR imaging: Quantitative evaluation of a novel model-based MR attenuation correction method including bone. *Journal of Nuclear Medicine*, 56(7):1061–1066.

Robson, M. D., Gore, J. C., and Constable, R. T. (1997). Measurement of the point spread function in MRI using constant time imaging. *Magnetic Resonance in Medicine*, 38(5):733–740.

Siversson, C., Nordstrom, F., Nilsson, T., Nyholm, T., Jonsson, J., Gunnlaugsson, A., and Olsson, L. E. (2015). Technical Note: MRI only prostate radiotherapy planning using the statistical decomposition algorithm. *Medical Physics*, 42(10):6090–6097.

Stanescu, T., Jans, H. S., Pervez, N., Stavrev, P., and Fallone, B. G. (2008). A study on the magnetic resonance imaging (MRI)-based radiation treatment planning of intracranial lesions. *Physics in Medicine Biology*, 53(13):3579–3593.

Veiga, C., Lourenco, A. M., Mouinuddin, S., van Herk, M., Modat, M., Ourselin, S., Royle, G., and McClelland, J. R. (2015). Toward adaptive radiotherapy for head and neck patients: Uncertainties in dose warping due to the choice of deformable registration algorithm. *Medical Physics*, 42(2):760–769.

Walker, A., Liney, G., Metcalfe, P., and Holloway, L. (2014). Mri distortion: considerations for mri based radiotherapy treatment planning. *Australasian Physical & Engineering Sciences in Medicine*, 37(1):103–113.

Walker, A., Metcalfe, P., Liney, G., Batumalai, V., Dundas, K., Glide-Hurst, C., Delaney, G. P., Boxer, M., Yap, M. L., Dowling, J., Rivest-Henault, D., Pogson, E., and Holloway, L. (2016). MRI geometric distortion: Impact on tangential whole-breast IMRT. *Journal of Applied Clinical Medical Physics*, 17(5):7–19.

Wang, D., Strugnell, W., Cowin, G., Doddrell, D. M., and Slaughter, R. (2004). Geometric distortion in clinical MRI systems Part I: evaluation using a 3D phantom. *Magnetic Resonance Imaging*, 22(9):1211–1221.

Wang, H., Balter, J., and Cao, Y. (2013). Patient-induced susceptibility effect on geometric distortion of clinical brain MRI for radiation treatment planning on a 3T scanner. *Physics in Medicine Biology*, 58(3):465–477.

Wang, H., Chandarana, H., Block, K. T., Vahle, T., Fenchel, M., and Das, I. J. (2017). Dosimetric evaluation of synthetic CT for magnetic resonance-only based radiotherapy planning of lung cancer. *Radiation Oncology*, 12(1):108.

Wang, H., Du, K., Qu, J., Chandarana, H., and Das, I. J. (2018). Dosimetric evaluation of magnetic resonance-generated synthetic CT for radiation treatment of rectal cancer. *PLoS ONE*, 13(1):e0190883.

Weygand, J., Fuller, C. D., Ibbott, G. S., Mohamed, A. S., Ding, Y., Yang, J., Hwang, K. P., and Wang, J. (2016). Spatial precision in magnetic resonance imaging-guided radiation therapy: The role of geometric distortion. *International Journal of Radiation Oncology, Biology, Physics*, 95(4):1304–1316.

Wiesinger, F., Bylund, M., Yang, J., Kaushik, S., Shanbhag, D., Ahn, S., Jonsson, J. H., Lundman, J. A., Hope, T., Nyholm, T., Larson, P., and Cozzini, C. (2018). Zero TE-based pseudo-CT image conversion in the head and its application in PET/MR attenuation correction and MR-guided radiation therapy planning. *Magnetic Resonance in Medicine*, 80(4):1440–1451.

APPENDIX

Table A1: Dose volume objectives from the ARTSCAN III protocol (Gebre-Medhin, 2013).

Priority	Volume	Objective (Gy)	Contraint (Gy)
1[1]	Spinal cord		$D_{max} \leq 46$
2[1]	PRV spinal cord		$D_{2\%} \leq 48$
3[1]	Brain steam		$D_{2\%} \leq 54$
4	GTVT68 and GTVN68	$D_{98\%} \geq 66$	
5	PTV 68	$D_{98\%} \geq 64.6$	
6	PTV 68[2]	$D_{2\%} \leq 71.4$	
7	PTV 73.1	$D_{98\%} \geq 70.9$	
8	PTV 73.1	$D_{2\%} \leq 76.8$	
9	PTV 54.4	$D_{98\%} \geq 51.7$	
10	Parotid glands	$D_{mean} \leq 25$ (both glands) $D_{mean} \leq 20$ (one gland)	
11	Larynx	$D_{mean} \leq 40$	
12	Pharynx	$D_{mean} \leq 50$	
13	Oral cavity	$D_{mean} \leq 24$	
14	Cochlea	$D_{mean} \leq 10$	
15	Upper esophageal sphincter	$D_{mean} \leq 40$	
16	Mandible	$D_{2\%} \leq 70$	
17	Submandibular glands	$D_{mean} \leq 39$	
18	External	$D_{max} \leq 72.8$[3] or $D_{max} \leq 78.2$[4]	

[1]Hard constraints
[2]Only applicable in patients that are NOT prescribed 73.1 Gy
[3]If prescribed 68 Gy
[4]If prescribed 73.1 Gy

Table A2: Original data showing the absorbed dose [Gy] for all patients, structures and their corresponding parameters for both D_{RTdist} and D_{RTref}.

Patient		CTV_{68} D_{mean}	CTV_{68} $D_{98\%}$	CTV_{68} $D_{2\%}$	$CTV_{52.7}$ $D_{98\%}$	PRV Spinal cord $D_{2\%}$	Parotid left D_{mean}	Parotid right D_{mean}	Larynx D_{mean}	Esophagus D_{mean}	Submandib. left D_{mean}	Submandib. right D_{mean}	Body D_{mean}
1	D_{RTdist}	68.295	65.221	70.729		29.720	45.354	5.851	37.191	39.729		37.330	75.466
	D_{RTref}	68.181	64.555	70.663		30.068	45.275	5.864	37.988	40.413		37.366	76.253
2	D_{RTdist}	68.713	67.145	70.145	50.713	42.600	14.671	20.821	68.839	37.724	44.799	68.724	71.822
	D_{RTref}	68.719	67.196	70.149	50.692	42.132	14.644	20.833	68.808	41.575	44.329	68.684	71.804
3	D_{RTdist}	68.497	64.749	70.483	50.365	42.037	18.782	37.975	39.143	39.345	59.215	68.684	73.928
	D_{RTref}	68.525	65.613	70.444	50.800	42.116	18.810	37.814	38.960	39.334	59.256	68.635	73.880
4	D_{RTdist}	68.615	65.89	71.107		42.507	12.313	52.346	26.267	6.999	21.681	68.850	73.434
	D_{RTref}	68.600	66.188	71.117		42.454	12.286	52.311	26.371	7.042	21.648	68.853	73.446
5	D_{RTdist}	68.382	66.545	70.366	50.927	43.737	22.524	32.767	50.743	48.800	51.741	68.546	76.120
	D_{RTref}	68.393	66.635	70.458	50.918	43.768	22.468	31.033	50.570	48.729	51.664	68.517	76.056
6	D_{RTdist}	68.089	65.305	69.936	49.556	42.892	24.799	18.230	37.347	32.715	67.023	37.876	72.424
	D_{RTref}	68.056	65.240	69.913	50.001	42.881	24.748	18.158	37.482	32.676	67.019	37.942	72.361
7	D_{RTdist}	68.537	65.881	70.522	51.076	42.823	19.763	25.162	45.986	32.893	58.437	68.118	73.312
	D_{RTref}	68.537	66.020	70.504	51.258	42.826	20.143	25.085	46.083	32.376	58.282	68.138	73.400
8	D_{RTdist}	68.612	67.385	69.881	51.765	40.158	31.212	21.154	39.246	13.203	60.890	42.550	72.441
	D_{RTref}	68.531	67.303	69.799	51.745	40.216	31.128	21.103	39.302	13.235	60.683	42.685	72.368
9	D_{RTdist}	69.011	67.291	70.980	47.663	44.851	15.752	29.995	47.695	37.453	62.865	69.157	73.280
	D_{RTref}	68.964	67.196	70.966	47.592	44.841	15.856	28.586	47.883	37.456	62.848	69.179	73.265
10	D_{RTdist}	67.545	60.577	69.361	50.755	38.446		7.510	30.772	20.446		13.098	72.149
	D_{RTref}	67.526	60.334	69.364	51.058	38.647		7.520	30.943	20.365		13.261	72.138